

# Commensurate $4a_0$ -period charge density modulations throughout the $\text{Bi}_2\text{Sr}_2\text{CaCu}_2\text{O}_{8+x}$ pseudogap regime

Andrej Mesaros<sup>a</sup>, Kazuhiro Fujita<sup>b</sup>, Stephen D. Edkins<sup>a,c</sup>, Mohammad H. Hamidian<sup>d,e</sup>, Hiroshi Eisaki<sup>f</sup>, Shin-ichi Uchida<sup>f,g</sup>, J. C. Séamus Davis<sup>a,b,c,h,1</sup>, Michael J. Lawler<sup>a,i</sup>, and Eun-Ah Kim<sup>a,1</sup>

<sup>a</sup>Laboratory of Atomic and Solid State Physics, Department of Physics, Cornell University, Ithaca, NY 14853; <sup>b</sup>Condensed Matter Physics and Materials Science Department, Brookhaven National Laboratory, Upton, NY 11973; <sup>c</sup>School of Physics and Astronomy, University of St. Andrews, St. Andrews, Fife KY16 9SS, Scotland; <sup>d</sup>Department of Physics, Harvard University, Cambridge, MA 02138; <sup>e</sup>Department of Physics, University of California, Davis, CA 95616; <sup>f</sup>Superconducting Electronics Group, Electronics and Photonics Research Institute, National Institute of Advanced Industrial Science and Technology, Tsukuba, Ibaraki 305-8568, Japan; <sup>g</sup>Department of Physics, University of Tokyo, Bunkyo-ku, Tokyo 113-0033, Japan; <sup>h</sup>Tyndall National Institute, University College Cork, Cork T12R5C, Ireland; and <sup>i</sup>Department of Physics, Binghamton University, Binghamton, NY 13902-6000

Contributed by J. C. Séamus Davis, September 1, 2016 (sent for review July 13, 2016; reviewed by Marc-Henri Julien and J. Zaanen)

Theories based upon strong real space ( $r$ -space) electron–electron interactions have long predicted that unidirectional charge density modulations (CDMs) with four-unit-cell ( $4a_0$ ) periodicity should occur in the hole-doped cuprate Mott insulator (MI). Experimentally, however, increasing the hole density  $p$  is reported to cause the conventionally defined wavevector  $Q_A$  of the CDM to evolve continuously as if driven primarily by momentum-space ( $k$ -space) effects. Here we introduce phase-resolved electronic structure visualization for determination of the cuprate CDM wavevector. Remarkably, this technique reveals a virtually doping-independent locking of the local CDM wavevector at  $|Q_0| = 2\pi/4a_0$  throughout the underdoped phase diagram of the canonical cuprate  $\text{Bi}_2\text{Sr}_2\text{CaCu}_2\text{O}_8$ . These observations have significant fundamental consequences because they are orthogonal to a  $k$ -space (Fermi-surface)–based picture of the cuprate CDMs but are consistent with strong-coupling  $r$ -space–based theories. Our findings imply that it is the latter that provides the intrinsic organizational principle for the cuprate CDM state.

$\text{CuO}_2$  pseudogap | commensurate charge density modulation | phase discommensuration

Strong Coulomb interactions between electrons on adjacent Cu sites result in complete charge localization in the cuprate Mott insulator (MI) state (1). When holes are introduced, theories based upon the same strong  $r$ -space interactions have long predicted a state of unidirectional modulation of spin and charge (2–11), with lattice-commensurate periodicity for the charge component. Experimentally, it is known that even the lightest hole doping of the MI state produces nanoscale clusters of charge density modulations (CDMs) (12, 13), which implies immediately that  $r$ -space interactions predominate. However, with increasing hole density  $p$ , the conventionally defined wavevector  $Q_A$  of the CDM is reported to increase (14) or diminish (15) continuously as if driven primarily by  $k$ -space (Fermi surface) effects. Distinguishing between the  $r$ -space and  $k$ -space theoretical perspectives is critical to identifying the correct fundamental theories for the phase diagram and Cooper pairing mechanism in underdoped cuprates. Here we introduce an approach to this challenge by applying phase-resolved electronic structure visualization (16–18) in combination with the technique of phase demodulation–residue minimization, to explore the CDM wavevector. Using these methods, we visualize the phase discommensurations (19) and their influence on the doping dependence of both the conventionally defined  $Q_A$  and the fundamental local wavevector  $Q_0$  of the underdoped cuprate CDM state.

## CDMs in the Pseudogap Phase

As holes are introduced into the  $\text{CuO}_2$  plane of the MI, the first nonmagnetic state to appear is the pseudogap (PG) phase (Fig. 1A). It contains nanoscale CDM clusters (12, 13) even at lowest hole-density  $p$ ; near  $p = 0.06$  these CDM clusters percolate and the superconducting state appears (12). X-ray scattering experiments (15) now report a robust CDM state throughout the range

$0.07 < p < 0.17$  spanning the pseudogap regime. Both the PG and the CDM states terminate somewhere near  $p \sim 0.19$  and give way to a simple d-wave superconductor. A fundamental reason for the great difficulty in understanding this complex phase diagram has been the inability to discern the correct theoretical starting point. Should one focus on the intense  $r$ -space electron–electron interactions that form the basis for the parent MI state? Or should one focus upon a Fermi surface of momentum space eigenstates representing delocalized electrons?

A new opportunity to address these questions has emerged recently, through studies of the CDM phenomena now widely observed in underdoped cuprates (15, 20, 21). Pioneering studies of CDMs in  $\text{La}_{2-x}\text{Ba}_x\text{CuO}_4$  and  $\text{La}_{2-x-y}\text{Nd}_y\text{Sr}_x\text{CuO}_4$  near  $p = 0.125$  discovered charge modulations of period  $4a_0$  or  $Q = ((1/4, 0); (0, 1/4))2\pi/a_0$  (14, 21). The initial intuitive explanation for a periodicity that was half that predicted from a Hartree–Fock momentum space treatment invoked an  $r$ -space model involving local magnetic moments whose antiferromagnetic order becomes frustrated upon hole doping. A variety of powerful theoretical techniques (2–11) support this strongly interacting  $r$ -space viewpoint. In the interim, however, CDM phenomena have been discovered within the pseudogap regime of many other underdoped cuprates (15, 20, 21).

## Significance

Strong Coulomb interactions between electrons on adjacent Cu atoms result in charge localization in the cuprate Mott-insulator state. When a few percent of electrons are removed, both high-temperature superconductivity and exotic charge density modulations appear. Identifying the correct fundamental theory for superconductivity requires confidence on whether a particle-like or a wave-like concept of electrons describes this physics. To address this issue, here we take the approach of using the phase of charge modulations, available only from atomic-scale imaging. It reveals a universal periodicity of the charge modulations of four crystal unit cells. These results indicate that the particle-like concept of strong interactions in real-space provides the intrinsic organizational principle for cuprate charge modulations, implying the equivalent for the superconductivity.

Author contributions: A.M., M.J.L., and E.-A.K. designed research; J.C.S.D. and E.-A.K. supervised the project; A.M., K.F., S.D.E., M.H.H., M.J.L., and E.-A.K. performed research; H.E. and S.-i.U. contributed new reagents/analytic tools; and A.M., K.F., J.C.S.D., M.J.L., and E.-A.K. wrote the paper.

Reviewers: M.-H.J., Laboratoire National des Champs Magnétiques Intenses–Grenoble; and J.Z., Leiden University.

The authors declare no conflict of interest.

Freely available online through the PNAS open access option.

<sup>1</sup>To whom correspondence may be addressed. Email: jkseamusdavis@gmail.com or eun-ah.kim@cornell.edu.

This article contains supporting information online at [www.pnas.org/lookup/suppl/doi:10.1073/pnas.1614247113/-DCSupplemental](http://www.pnas.org/lookup/suppl/doi:10.1073/pnas.1614247113/-DCSupplemental).

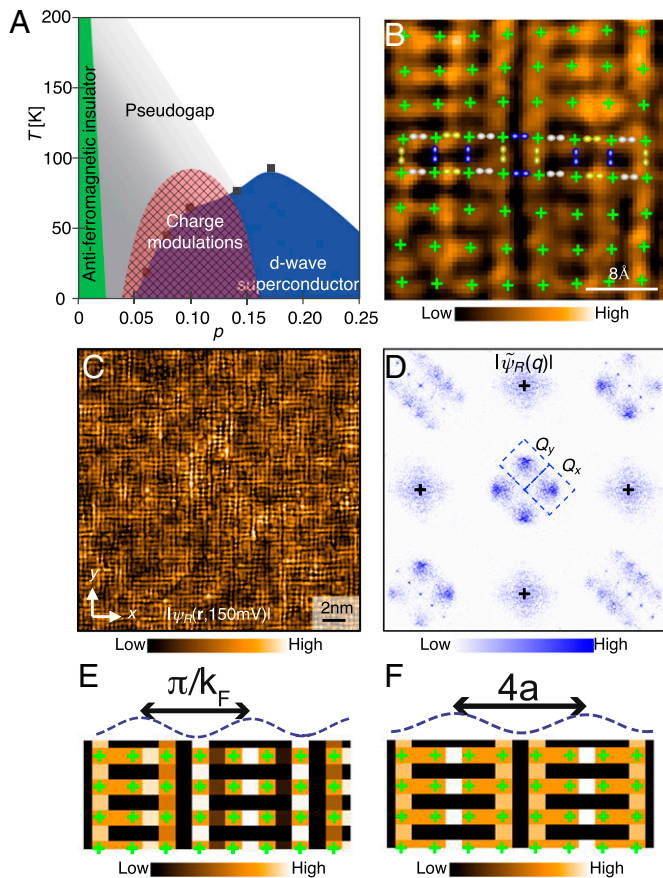


**Fig. 1.** (A) Schematic phase diagram of hole-doped cuprates. The high-temperature superconductivity coexists with  $d$ -symmetry form factor charge modulations (compare blue and pink “domes,” respectively) through most of the underdoped regime. (B) Typical measured  $\psi_R(\mathbf{r}, 150 \text{ meV})$  image of  $\text{Bi}_2\text{Sr}_2\text{CaCu}_2\text{O}_{8+x}$  in the charge modulation phase. The subatomic resolution image shows a typical charge modulation pattern of  $d$ -symmetry form factor, spanning eight lattice constants horizontally (compare with E and F), and with an overlay showing how the  $d$ -symmetry form factor affects each oxygen site. The green crosses mark positions of Cu atoms in the underlying  $\text{CuO}_2$  plane. (C) Typical  $\psi_R(\mathbf{r}, 150 \text{ meV})$  of underdoped  $\text{Bi}_2\text{Sr}_2\text{CaCu}_2\text{O}_{8+x}$ . The short-range nature of the charge modulations is clear. (D) The  $d$ -symmetry form factor Fourier amplitudes  $|\tilde{\psi}_R(\mathbf{q}, 150 \text{ meV})|$  calculated using complex Fourier transforms of sublattice-resolved images  $O_x(\mathbf{r}); O_y(\mathbf{r})$  derived from C. (E) Modeled  $d$ -form factor charge density wave that represents an incommensurate modulation by having a horizontal wavevector of length  $Q = 0.311 \times 2\pi/a$ , where  $a$  is the lattice unit. The density values are sampled and color coded at each Cu site (green crosses), O site, and center of  $\text{CuO}_2$  plaquette, to emphasize the modulation pattern and relation to the underlying lattice. The initial phase is chosen so that the modulation on the leftmost line of Cu sites matches in value the commensurate modulation in F. Incommensurate modulations such as the one shown naturally arise from Fermi surface instabilities and therefore have the Fermi surface nesting wavevector  $Q = 2k_F$  and period  $2\pi/Q = \pi/k_F$ . The dashed line is the profile of the density wave along the horizontal direction, without imposing a  $d$ -form factor intraunit-cell structure, and the period is marked by the length of the double arrow. (F) Modeled  $d$ -form factor charge density wave that is commensurate, having wavevector  $Q = 1/4 \times 2\pi/a$  and period  $2\pi/Q = 4a$  with  $a$  the lattice unit. The density values are sampled and color coded at each Cu site (green crosses), O site, and center of  $\text{CuO}_2$  plaquette, to emphasize the modulation pattern and relation to the underlying lattice. The initial wave phase is chosen so that the modulation maximum occurs on a horizontal O site. The dashed line is the profile of the density wave along the horizontal direction and the period is marked by the length of the double arrow.

In these studies, the magnitude of the conventionally determined CDM wavevector  $Q$  is reported to increase/diminish with increasing  $p$ , as if evolution of momentum space electronic structure

with carrier density is the cause. Thus, distinguishing between an  $r$ -space-based and a Fermi-surface-based theoretical approach to the cuprate CDM remains an outstanding and fundamental challenge and one that is key to the larger issue of controlling the balance between different electronic phases. The reason is that, in the  $k$ -space context (22–25), competition for spectral weight at the Fermi surface between different electronic states including the superconductivity is a zero sum game: Suppressing one state amplifies another and vice versa. By contrast, in the strong interaction  $r$ -space context (2–11), the physics of holes doped into an antiferromagnetic MI yield “intertwined” states (4, 8–11, 26, 27) including superconductivity, where closely related ordered states are generated simultaneously by the same microscopic interactions.

### CDMs and Phase Discommensurations

Understanding the cuprate CDM phenomenology has proved challenging (28–30) because its  $q$ -space peaks are typically broad with spectral weight distributed over many wavevectors (15–21) and also because of the form factor symmetry (17, 31–33). For example, Fig. 1 B and C shows a typical image of the electronic structure of underdoped  $\text{Bi}_2\text{Sr}_2\text{CaCu}_2\text{O}_{8+x}$   $\psi_R(\mathbf{r})$ ; here  $\psi_R(\mathbf{r}, 150 \text{ meV}) \equiv I(\mathbf{r}, 150 \text{ meV})/I(\mathbf{r}, -150 \text{ meV})$  and  $I(\mathbf{r}, V)$  is the measured tunnel current at position  $\mathbf{r}$  for bias voltage  $V$ . The CDM exhibits a  $d$ -symmetry form factor meaning that modulations at the  $x$ -axis-oriented planar oxygen sites  $O_x(\mathbf{r})$  are  $\pi$  out of phase with those at  $y$ -axis-oriented oxygen sites  $O_y(\mathbf{r})$ , as shown schematically by the overlay in Fig. 1B. Thus, the complex Fourier transforms  $\tilde{O}_x(\mathbf{q}); \tilde{O}_y(\mathbf{q})$  of sublattice-resolved images  $O_x(\mathbf{r}); O_y(\mathbf{r})$  that are derived (17, 33) from  $\psi_R(\mathbf{r})$  yield the  $d$ -symmetry form factor Fourier amplitudes  $|\tilde{\psi}_R(\mathbf{q})| = |\tilde{O}_x(\mathbf{q}) - \tilde{O}_y(\mathbf{q})|$  shown in Fig. 1D (SI Text, *d*-Symmetry Form Factor of CDMs). One sees directly the wide range of  $q$  values that exist under each CDM peak in  $\tilde{\psi}_R(\mathbf{q})$  (dashed boxes, Fig. 1D). Such broad peaks indicate quenched disorder of the CDM but with two quite distinct possibilities for the identity of the fundamental ordered state: (i) an incommensurate CDM state whose wavevector  $Q$  evolves continuously along with the Fermi wavevector  $k_F$  (e.g., Fig. 1E) but is perturbed by disorder or (ii) a commensurate CDM with constant fundamental wavevector  $Q_0$  driven by strong-coupling  $r$ -space effects (e.g., Fig. 1F), but whose wavevector defined at the maximum of the fitted Fourier amplitudes,  $Q_A$ , evolves due to changing arrangements of discommensurations (DC).

McMillan (19) defined a “discommensuration” as a defect in a commensurate CDM state where the phase of the CDM jumps between discrete lattice-locked values. For example, consider a sinusoidal modulation in one spatial dimension with a commensurate period  $4a_0$ :

$$\psi(x) \equiv A \exp[i\Phi(x)] = A \exp[i(Q_0x + \varphi)]. \quad [1]$$

Here  $Q_0 = 2\pi/4a_0$  is the commensurate wavevector,  $A$  is the amplitude, and  $\Phi(x) = Q_0x + \varphi$  is the position-dependent phase argument of the function  $\psi(x)$ . To form phase-locked regions, the phase offset can take one of four discrete values  $\frac{\varphi}{2\pi} = 0, \frac{1}{4}, \frac{2}{4}, \frac{3}{4}$ . The DCs then form boundaries between these regions as indicated by different colors in Fig. 2 A, *i* and *ii*. When a commensurate CDM (Eq. 1) is frustrated by Fermi-surface-based tendencies, a regular DC array allows more/fewer modulations to be accommodated through successive jumps in phase (Fig. 2 A, *ii* and ref. 19). The result is a new phase-averaged wavevector  $\bar{Q}$  that depends on the profile of the DC array  $\varphi(x)$  through  $Q_0x + \varphi(x) \equiv \bar{Q}x + \tilde{\varphi}(x)$ , where the slope  $\bar{Q}$  is chosen so that the residual phase fluctuations  $\tilde{\varphi}(x)$  average to zero ( $\overline{\tilde{\varphi}(x)} = 0$ ). Graphically, finding the  $\bar{Q}$  is then equivalent to finding the best linear function for  $\Phi(x)$  as shown in Fig. 2 A, *ii*. In this case, the difference in slope between the commensurate and phase-averaged wavevectors,  $Q_0$  and  $\bar{Q}$ , is called the incommensurability  $\delta \equiv \bar{Q} - Q_0$  (Fig. 2 A, *iii*) of such a nominally incommensurate phase.

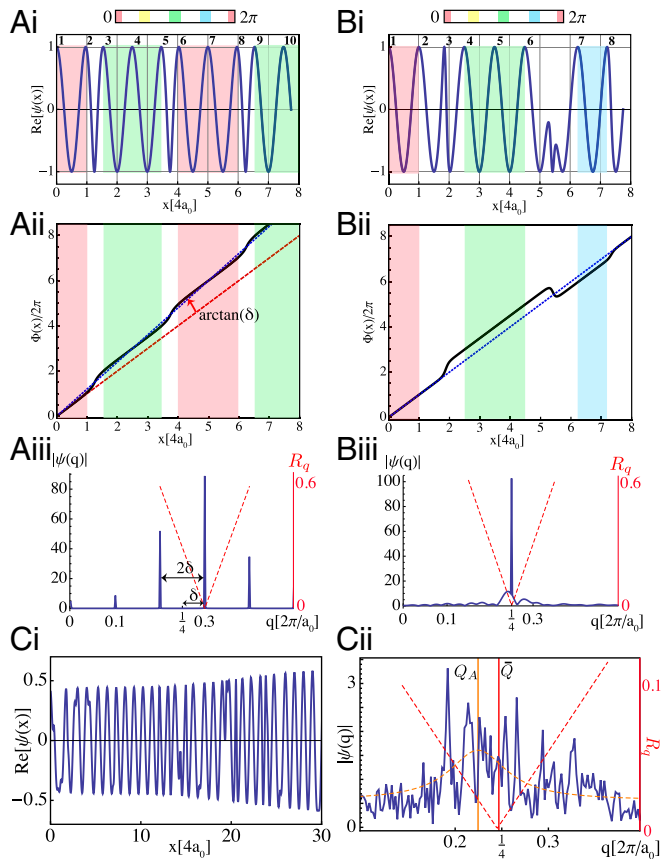


**Fig. 2.** *A, i–iii* shows a DC model in a situation that may apply to  $\text{YBa}_2\text{Cu}_3\text{O}_{7-x}$ . The model in *B* and *C* corresponds to our findings in  $\text{Bi}_2\text{Sr}_2\text{CaCu}_2\text{O}_{8+x}$  (BSCCO). (*A, i*) Modulation (blue, thick line) is the real part of complex wave  $\psi(x) = e^{i(Q_0 x + \varphi(x))}$  having commensurate domains with local wavevector  $Q_0 = 1/4 \times 2\pi/a_0$  (period  $4a_0$ ). Colors (see key on top) label the modulation phase within the domains, determining the alignment of modulation maxima (labeled 1...10) and underlying lattice. Phase slips, occurring at DCs between domains, each of size  $\pi$ , add up to give an average  $\bar{Q} = 0.3 \times 2\pi/a_0$ , so that 10 modulation maxima are squeezed into  $31a_0$ . (*A, ii*) The phase argument  $\Phi(x) = Q_0 x + \varphi(x)$  of  $\psi(x)$  in *A, i*. Commensurate domains occur in regions (colored) where  $\Phi(x)$  is parallel to line  $Q_0 x$  (red dashed line). The average  $\bar{Q} = 0.3 \times 2\pi/a_0$  is seen as a slope of the best-fit line to  $\Phi(x)$  (blue dashed line). The difference in slope gives the incommensurability  $\delta = \bar{Q} - Q_0$ . (*A, iii*) Fourier amplitudes  $|\tilde{\psi}(q)|$  of the modulation  $\psi(x)$  in *A, i* (blue line) show singular peaks starting at  $\bar{Q} = 0.3 \times 2\pi/a_0 \neq Q_0$  with satellites separated by  $2\delta$ , because DCs of size  $\pi$  form a periodic array. The satellites depend on DC profile and are sensitive to disorder (*SI Text, Heterogeneity and Demodulation Residue*). The phase-sensitive figure of merit, demodulation residue  $|R_q|$  (red dashed line), as a function of  $q$  has the minimum exactly at the average  $\bar{Q}$ . By definition its minimum corresponds to the slope of the best-fit line through  $\Phi(x)$  (*A, ii*). (*B, i*) Modulation (blue, thick line) is the real part of complex wave  $\psi(x) = e^{i(Q_0 x + \varphi(x))}$  having commensurate domains with fundamental local wavevector  $Q_0 = 1/4 \times 2\pi/a_0$  (period  $4a_0$ ). Colors label the modulation phase within the domains, determining the alignment of modulation maxima (labeled 1...8) and underlying lattice. All of the phase slips, of sizes  $+\pi$ ,  $-(3\pi/2)$ ,  $+(\pi/2)$ , occurring at DCs between domains, cancel to give an average  $\bar{Q} = Q_0$ , seen in preserving the eight modulation maxima within  $31a_0$ . (*B, ii*) The phase argument  $\Phi(x) = Q_0 x + \varphi(x)$  of  $\psi(x)$  in *B, i*. Commensurate domains occur in regions (colored) where  $\Phi(x)$  is parallel to line  $Q_0 x$  (blue dashed line). The average  $\bar{Q} = Q_0$  is seen as the slope of the best-fit line to  $\Phi(x)$ , which coincides with the dashed line. (*B, iii*) Fourier amplitudes  $|\tilde{\psi}(q)|$  of the modulation  $\psi(x)$  in *B, i* (blue line) have a sharp peak at  $\bar{Q} = Q_0$  and additional irregularly distributed weight due to disorder in DC's position (*SI Text, Heterogeneity and Demodulation Residue*). The calculated phase-sensitive figure of merit, demodulation residue  $|R_q|$  (red dashed line), as a function of  $q$  has the minimum exactly at the average  $\bar{Q}$ . By definition its minimum corresponds to the slope of the best-fit line through  $\Phi(x)$  (*B, ii*). (*C, i*) Modulation (blue, thick line) is the real part of complex wave

Note that such a DC array does not affect the correlation length of the CDM even though it does shift the Fourier amplitude-defined wavevector  $Q_A$  to value  $\bar{Q}$  from the fundamental commensurate wavevector  $Q_0$  (Fig. 2 *A, iii*). In contrast, when the combined phase jumps of all of the DCs average to zero (Fig. 2 *B, i* and *ii*), the phase-averaged wavevector  $\bar{Q}$  equals the local commensurate wavevector; i.e.,  $\bar{Q} = Q_0$ . Here, in the absence of additional amplitude disorder, the  $Q_A$  should also peak at  $\bar{Q} = Q_0$  (Fig. 2 *B, iii*). However, in the most realistic case where disorder in the CDM amplitude and the random spatial arrangement of DCs coexist,  $Q_A$  is demonstrably a poor measure of the fundamental commensurate wavevector  $\bar{Q} = Q_0$  (Fig. 2 *C, i* and *ii*; *SI Text, Heterogeneity and Demodulation Residue*; and *SI Text, Statistical Analysis: Two-Dimensional Fitting*).

How then can one correctly determine the fundamental  $Q_0$  of the CDMs in underdoped cuprates? The spatial arrangement of DCs is inaccessible to diffraction probes designed to yield the Fourier amplitude of the CDM, although the situation in Fig. 2 *A, iii* may be detectable through the observation of satellite peaks at  $\bar{Q} \pm \delta$  (*SI Text, Heterogeneity and Demodulation Residue*; and *SI Text, CDM Commensurability in Underdoped BSCCO*). Phase-sensitive transmission electron microscopy can achieve DC visualization (34), whereas coherent X-ray diffraction might (35), but neither one has been used on cuprates. Instead, we consider CDM visualization using spectroscopic imaging scanning tunneling microscopy (20) because it offers full access to both the amplitude and phase of  $\tilde{\psi}(q)$ , with the definition of phase referenced to the underlying atomic lattice (33). Then, based on such phase visualization capabilities, we introduce an approach for identifying the fundamental wavevector of the cuprate CDM state. To achieve what is graphically represented in Fig. 2 as the dashed linear fit to a measured phase profile  $\Phi(x)$ , we use an algorithmic procedure that evaluates the demodulation of measured CDM image  $\psi(\mathbf{r})$  at each possible wavevector  $q$ , using the demodulation residue

$$R_q[\psi] \equiv \int \frac{dx}{L} \text{Re} \left[ \psi_q^*(x) (-i\partial_x) \psi_q(x) \right]. \quad [2]$$

Identifying the value of wavevector  $q$  for which  $|R_q[\psi]|$  is a minimum is the 2D equivalent to finding the best-fit slope to  $\Phi(x)$  in Fig. 2 *A* and *B*. The resulting wavevector  $q = \bar{Q}$  with high accuracy (*SI Text, Heterogeneity and Demodulation Residue*), and determination of this  $\bar{Q}$  is the general objective and utility of this technique.

### Phase-Resolved Imaging and Phase Demodulation Residue Analysis

We apply demodulation residue analysis to study 2D short-range ordered CDM images typical of underdoped  $\text{Bi}_2\text{Sr}_2\text{CaCu}_2\text{O}_{8+x}$ , e.g., Fig. 3*A* at  $p = 0.06$ . Fig. 3*B* shows the  $d$ -symmetry form factor Fourier amplitude  $|\tilde{\psi}(q)|$  derived from  $\psi(\mathbf{r})$  in Fig. 3*A*. The amplitude and phase of modulations in  $\psi(\mathbf{r})$  can be decomposed into two unidirectional components along  $x, y$ . We define the demodulation residue  $R_q$  for each trial  $q$  (*SI Text, Demodulation in Two Dimensions, Smoothing, and Optimization Error*) over a wide range in the Fourier space inside the dashed box in Fig. 3*B* and

$\psi(x) = A(x)e^{i(Q_0 x + \varphi(x))}$  having commensurate domains with local wavevector  $Q_0 = 1/4 \times 2\pi/a_0$ , additional smooth disorder in phase of up to  $\pi/10$ , and smooth disorder in amplitude  $A(x)$  (details in *SI Text, Heterogeneity and Demodulation Residue*). All random phase slips cancel to give a  $\bar{Q} = Q_0$ , akin to the case in *B*. (*C, ii*) Fourier amplitudes  $|\tilde{\psi}(q)|$  of modulation  $\psi(x)$  over  $125a_0$  range (exemplified in *C, i*). The broad asymmetric amplitude peak makes the  $Q_A$  (orange vertical line), at maximum of Lorentzian fit to amplitude (orange dashed line, multiplied by 1.5 for visibility), different from phase-averaged  $\bar{Q}$  (red vertical line) at minimum of demodulation residue  $|R_q|$  (red dashed line) (*SI Text, Heterogeneity and Demodulation Residue*).



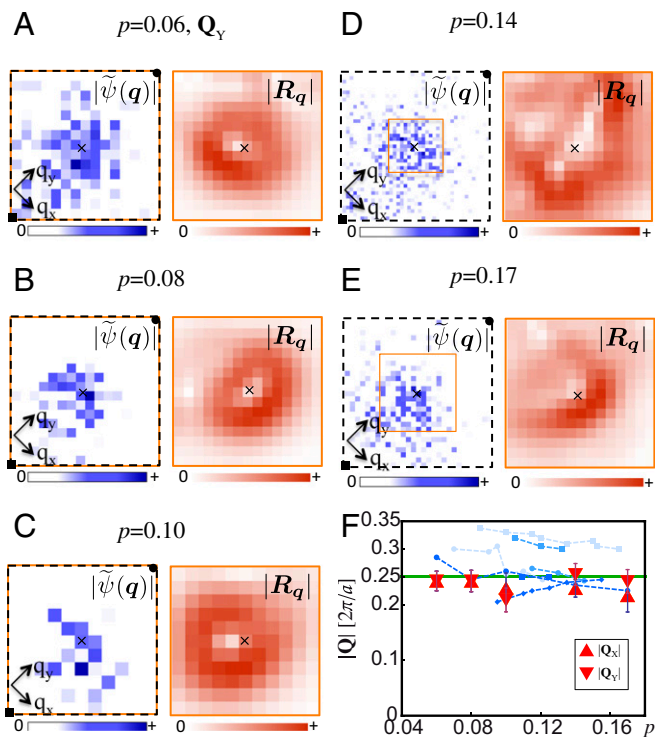


**Fig. 4.** (A, Left) Measured  $|\tilde{\psi}(\mathbf{q})|$  for  $p = 0.06$ , within the square region of  $\mathbf{q}$  space (the dashed square in Fig.3B) bounded by  $(0,0), (\pi/2a_0, \pi/2a_0), (0, \pi/a_0), (-\pi/2a_0, \pi/2a_0)$ . (A, Right) The value of demodulation residue  $|R_{\mathbf{q}}| = \sqrt{(R_x^y)^2 + (R_y^x)^2}$  calculated from data using cutoff  $\Lambda = 0.08 \times 2\pi/a_0$ . The measured  $|R_{\mathbf{q}}|$  varies smoothly and drops quickly toward zero at a single discrete wavevector near the center of the image, similar to behavior in one dimension (Fig. 2). The identified discrete wavevector has length  $|Q| = 0.245 \times 2\pi/a_0$ . The position of  $(0, 1/4) \times 2\pi/a_0$  is marked by a small cross. The same analysis as shown in A, but for a series of samples with estimated hole densities  $p = 0.08, 0.10, 0.14, 0.17$ . In each case in B–E, Left, shown is the measured  $|\tilde{\psi}(\mathbf{q})|$  within the square region of  $\mathbf{q}$  space that defines the considered CDM orientation, e.g., for  $Q_Y$  bounded by  $(0,0), (\pi/2a_0, \pi/2a_0), (0, \pi/a_0), (-\pi/2a_0, \pi/2a_0)$ ; in each case in B–E, Right, shown is the measured  $|R_{\mathbf{q}}|$  within the square region of  $\mathbf{q}$  space marked by the orange thin square on the image to its Left. The corresponding position of  $(0, 1/4) \times 2\pi/a_0$  is marked by a small cross. The pixel at which the  $|R_{\mathbf{q}}|$  is found to be a minimum is identified as the phase-optimized CDM wavevector for that carrier density. (F) The lengths of wavevectors  $Q_x, Q_y$  extracted from measured  $\text{Bi}_2\text{Sr}_2\text{CaCu}_2\text{O}_{8+x}$  underdoped samples at different dopings  $p$  using  $|R_{\mathbf{q}}|$  minimization (A–E). The error in value of the phase-optimized wavevector is obtained from spatial variation of residue (SI Text, Demodulation in Two Dimensions, Smoothing, and Optimization Error) and is comparable to the error caused by discreteness of choices for  $Q$ . For doping  $p > 0.14$  the  $d$ -form factor CDMs are less pronounced and there is a larger error in value of phase-optimized  $Q$ . Note the doping-independent trend and values consistent with commensurate value  $1/4$ . Shown are reported doping-dependent values of CDM wavevector length  $|Q_A|$  in  $\text{Bi}_2\text{Sr}_2\text{CaCu}_2\text{O}_{8+x}$  and  $\text{Bi}_2\text{Sr}_{2-x}\text{La}_x\text{CuO}_{6+y}$  (disks, colored light to dark in order for refs. 43, 44, and 33),  $\text{YBa}_2\text{Cu}_3\text{O}_{7-x}$  (squares, light to dark for source 132 from refs.15, 45, and 37), and  $\text{La}_{2-x}\text{Ba}_x\text{CuO}_4$  (diamonds, reported in ref. 45).

summarized in Fig. 4F is that the measured magnitudes of the average wavevectors  $Q_x, Q_y$  of the  $\text{Bi}_2\text{Sr}_2\text{CaCu}_2\text{O}_{8+x}$  CDM are all indistinguishable from the lattice commensurate values  $Q_0 = (0, 1/4)2\pi/a_0; (1/4, 0)2\pi/a_0$ , making the fundamental wavevectors  $Q_x, Q_y$  equal to  $Q_0$  and virtually doping independent (SI Text, Summary of Results for All Samples). Moreover, the largest deviation of the conventional amplitude-derived  $Q_A$  from the phase-optimized value  $Q = Q_0$  is at lowest doping, which can be associated with the observed higher density of DCs at the same doping (SI Text, Heterogeneity and Demodulation Residue).

## Ubiquity of Lattice-Commensurate CDMs

Comparison of this result with reports of a preference for a CDM periodicity of  $4a_0$  in  $\text{YBa}_2\text{Cu}_3\text{O}_{7-x}$ -based heterostructures (36), in the NMR-derived view of the lattice-commensurate CDM in  $\text{YBa}_2\text{Cu}_3\text{O}_{7-x}$  (37), and in the pair density wave state of  $\text{Bi}_2\text{Sr}_2\text{CaCu}_2\text{O}_{8+x}$  (38) points to growing evidence for a unified phenomenology of lattice-commensurate CDMs across disparate cuprate families. Of course, the wavevectors  $Q_A$  of maximum intensity in X-ray diffraction patterns for  $\text{YBa}_2\text{Cu}_3\text{O}_{7-x}$  and  $\text{La}_2\text{Sr}(\text{Ba})\text{CuO}_4$  families evolve continuously with doping and appear generally incommensurate (14, 15). However, DC configurations of the type in Fig. 2A will result in such an incommensurate average wavevector  $Q = Q_A$  even though the fundamental wavevector  $Q_0$  of the CDM is commensurate, so that evolution of cuprate DC arrays (e.g., Fig. 2) can yield the incommensurate wavevector evolution detected by X-ray scattering (SI Text, Global CDM Lattice Commensurability); a related hypothesis has long been considered (39). Our application of the classic theory of CDM DC disorder (19) (Fig. 2) with CDM phase-resolved imaging and analysis reveals this as the correct picture for  $\text{Bi}_2\text{Sr}_2\text{CaCu}_2\text{O}_{8+x}$ . This finding motivates the hypothesis that doping dependence of  $Q_A$  across all cuprate families is caused by a competition between incommensurate modulations promoted by evolving Fermi arcs and a lattice-commensurate CDM state, with this competition being resolved through DC configurations.

The  $|R_{\mathbf{q}}|$ -minimization technique introduced here is designed to use the additional CDM information available only from phase-resolved imaging (16, 17, 33). Remarkably, it reveals a doping-independent locking of the phase-averaged CDM wavevector to a lattice commensurate wavevector  $|Q_0| = 2\pi/4a_0$  oriented with the Cu-O-Cu bonds in  $\text{Bi}_2\text{Sr}_2\text{CaCu}_2\text{O}_{8+x}$  (Fig. 4). Moreover, we directly detect the CDM DCs between phase-locked commensurate regions that generate this situation (Fig. 3F). These observations have significant fundamental consequences for understanding the mechanism of the cuprate CDM state. They are orthogonal to a weak-coupling  $k$ -space-based picture for CDM phenomena, in which the fundamental wavevector should increase or decrease monotonically with doping or should evolve in discrete jumps even with “lattice locking.” Moreover, the commensurability is intractable as a perturbative effect of interactions in the  $k$ -space picture (40). By contrast, a lattice-commensurate CDM state has been obtained comprehensively in different types of strong-coupling  $r$ -space-based theories (2–11). For underdoped  $\text{Bi}_2\text{Sr}_2\text{CaCu}_2\text{O}_{8+x}$  at least, our data are far more consistent with such lattice-commensurate strong-coupling  $r$ -space theories being the intrinsic organizational principle for the cuprate CDM phenomena. Furthermore, nanoscale clusters of lattice-commensurate CDMs are the first broken-symmetry state to emerge at lightest hole doping (12, 13), multiple transport and spectroscopic measurements of cuprate quasiparticles have recently been demonstrated to be quite consistent with lattice-commensurate  $r$ -space theories (41), and  $\text{YBa}_2\text{Cu}_3\text{O}_{7-x}$  NMR studies (37, 42) are also most consistent with them. Explorations of universality of lattice commensurability of CDMs in other cuprate compounds can now be pursued using these phase-resolved imaging and  $|R_{\mathbf{q}}|$ -minimization techniques.

**ACKNOWLEDGMENTS.** A.M. acknowledges support from the US Department of Energy, Office of Basic Energy Sciences, Division of Materials Science and Engineering, under Award DE-SC0010313; E.-A.K. acknowledges Simons Fellow in Theoretical Physics Award 392182; S.D.E. acknowledges funding from Engineering and Physical Sciences Research Council Grants EP/G03673X/1 and EP/1031014/1; M.H.H. acknowledges support from the Moore Foundation’s Emergent Phenomena in Quantum Systems Initiative Grant GBMF4544; S.-i.U. and H.E. acknowledge support from a Grant-in-Aid for Scientific Research from the Ministry of Science and Education (Japan) and the Global Centers of Excellence Program for the Japan Society for the Promotion of Science. J.C.S.D. acknowledges gratefully the hospitality and support of the Tyndall National Institute, University College Cork. Experimental studies were supported by the Center for Emergent Superconductivity, an Energy Frontier Research Center, headquartered at Brookhaven National Laboratory and funded by US Department of Energy Grant DE-2009-BNL-PM015.

- Zaenán J, Sawatzky GA, Allen JW (1985) Band gaps and electronic structure of transition-metal compounds. *Phys Rev Lett* 55(4):418–421.
- Zaenán J, Gunnarsson O (1989) Charged magnetic domain lines and the magnetism of high- $T_c$  oxides. *Phys Rev B Condens Matter* 40(10):7391–7394.
- Löw U, Emery VJ, Fabricius K, Kivelson SA (1994) Study of an Ising model with competing long- and short-range interactions. *Phys Rev Lett* 72(12):1918–1921.
- Kivelson SA, Fradkin E, Emery VJ (1998) Electronic liquid-crystal phases of a doped Mott insulator. *Nature* 393(11):550–553.
- Vojta M, Sachdev S (1999) Charge order, superconductivity, and a global phase diagram of doped antiferromagnets. *Phys Rev Lett* 83(19):3916–3919.
- White SR, Scalapino DJ (1998) Density matrix renormalization group study of the striped phase in the 2D  $t$ - $J$  model. *Phys Rev Lett* 80(6):1272–1275.
- Capponi S, Poilblanc D (2002) Charge density correlations in  $t$ - $J$  ladders investigated by the contractor-renormalization method. *Phys Rev B* 66(18):180503–180503-4.
- Himeda A, Kato T, Ogata M (2002) Stripe states with spatially oscillating  $d$ -wave superconductivity in the two-dimensional  $t$ - $t'$ - $J$  model. *Phys Rev Lett* 88(11):117001–117004.
- Raczkowski M, Capello M, Poilblanc D, Frésard R, Oleś AM (2007) Unidirectional  $d$ -wave superconducting domains in the two-dimensional  $t$ - $J$  model. *Phys Rev B* 76(14):140505–140505-4.
- Loder F, Graser S, Kampf AP, Kopp T (2011) Mean-field pairing theory for the charge-stripe phase of high-temperature cuprate superconductors. *Phys Rev Lett* 107(18):187001.
- Corboz P, Rice TM, Troyer M (2014) Competing states in the  $t$ - $J$  model: Uniform  $D$ -wave state versus stripe state. *Phys Rev Lett* 113(4):046402–046405.
- Kohsaka Y, et al. (2012) Visualization of the emergence of the pseudogap state and the evolution to superconductivity in a lightly hole-doped Mott insulator. *Nat Phys* 8(7):534–538.
- Cai P, et al. (2015) Visualizing the evolution from the Mott insulator to a charge ordered insulator in lightly doped cuprates. *arXiv:1508.05586*.
- Hücker M, et al. (2011) Stripe order in superconducting  $\text{La}_{2-x}\text{Ba}_x\text{CuO}_4$  ( $0.095 < x < 0.155$ ). *Phys Rev B* 83(10):104506–104506-16.
- Comin R, Damascelli A (2016) Resonant x-ray scattering studies of charge order in cuprates. *Annu Rev Condens Matter Phys* 7:369–405.
- Slezak JA, et al. (2008) Imaging the impact on cuprate superconductivity of varying the interatomic distances within individual crystal unit cells. *Proc Natl Acad Sci USA* 105(9):3203–3208.
- Fujita K, et al. (2014) Direct phase-sensitive identification of a  $d$ -form factor density wave in underdoped cuprates. *Proc Natl Acad Sci USA* 111(30):E3026–E3032.
- Mesaros A, et al. (2011) Topological defects coupling smectic modulations to intra-unit-cell nematicity in cuprates. *Science* 333(6041):426–430.
- McMillan WL (1976) Theory of discommensurations and the commensurate-incommensurate charge-density-wave phase transition. *Phys Rev B* 14(4):1496–1502.
- Fujita K, et al. (2014) Spectroscopic imaging STM: Atomic-scale visualization of electronic structure and symmetry in underdoped cuprates. *Strongly correlated systems - Experimental Techniques*, Springer Series in Solid-State Sciences (Springer, Berlin), Vol 180, pp 73–109.
- Fradkin E, Kivelson SA, Tranquada JM (2015) Colloquium: Theory of intertwined orders in high temperature superconductors. *Rev Mod Phys* 87(2):457–482.
- Metlitski MA, Sachdev S (2010) Instabilities near the onset of spin density wave order in metals. *New J Phys* 12(10):105007–105007-13.
- Efetov KB, Meier H, Pépin C (2013) Pseudogap state near a quantum critical point. *Nat Phys* 9(7):442–446.
- Pépin C, de Carvalho VS, Kloss T, Montiel X (2014) Pseudogap, charge order, and pairing density wave at the hot spots in cuprate superconductors. *Phys Rev B* 90(19):195207–195207-16.
- Wang Y, Agterberg DF, Chubukov A (2015) Coexistence of charge-density-wave and pair-density-wave orders in underdoped cuprates. *Phys Rev Lett* 114(19):197001–197006.
- Davis JC, Lee DH (2013) Concepts relating magnetic interactions, intertwined electronic orders, and strongly correlated superconductivity. *Proc Natl Acad Sci USA* 110(44):17623–17630.
- Berg E, Fradkin E, Kivelson SA, Tranquada JM (2009) Striped superconductors: How spin, charge and superconducting orders intertwine in the cuprates. *New J Phys* 11(11):115004–115004-38.
- Robertson JA, et al. (2006) Distinguishing patterns of charge order: Stripes or checkerboards. *Phys Rev B* 74(13):134507–134507-10.
- Del Maestro A, et al. (2006) From stripe to checkerboard ordering of charge-density waves on the square lattice in the presence of quenched disorder. *Phys Rev B* 74(2):024520–1–024520-10.
- Phillabaum B, Carlson EW, Dahmen KA (2012) Spatial complexity due to bulk electronic nematicity in a superconducting underdoped cuprate. *Nat Commun* 3:915.
- Forgan EM, et al. (2015) The nature of the charge density waves in under-doped  $\text{YBa}_2\text{Cu}_3\text{O}_{6.54}$  revealed by X-ray measurements of the ionic displacements. *arXiv:1504.01585*.
- Comin R, et al. (2015) Symmetry of charge order in cuprates. *Nat Mater* 14(8):796–800.
- Hamidian MH, et al. (2016) Atomic-scale electronic structure of the cuprate  $d$ -symmetry form factor density wave state. *Nat Phys* 12(2):150–156.
- Chen CH, Gibson JM, Fleming RM (1981) Direct observation of charge-density-wave discommensurations and dislocations in 2H-TaSe<sub>2</sub>. *Phys Rev Lett* 47(10):723–725.
- Le Bolland D, et al. (2005) Charge density wave dislocation as revealed by coherent x-ray diffraction. *Phys Rev Lett* 95(11):116401–116404.
- He J, et al. (2016) Observation of a three-dimensional quasi-long-range electronic supermodulation in  $\text{YBa}_2\text{Cu}_3\text{O}_{7-x}/\text{La}_{0.7}\text{Ca}_{0.3}\text{MnO}_3$  heterostructures. *Nat Commun* 7:10852.
- Wu T, et al. (2011) Magnetic-field-induced charge-stripe order in the high-temperature superconductor  $\text{YBa}_2\text{Cu}_3\text{O}_y$ . *Nature* 477(7363):191–194.
- Hamidian MH, et al. (2016) Detection of a Cooper-pair density wave in  $\text{Bi}_2\text{Sr}_2\text{CaCu}_2\text{O}_{8+x}$ . *Nature* 532(7599):343–347.
- Tranquada JM, Ichikawa N, Uchida S (1999) Glassy nature of stripe ordering in  $\text{La}_{1.6-x}\text{Nd}_{0.4}\text{Sr}_x\text{CuO}_4$ . *Phys Rev B* 59(22):14712–14722.
- Mukhin SI, Matveenko SI (2003) Stripe phase: Analytical results for weakly coupled repulsive Hubbard model. *Int J Mod Phys B* 17(21):3749–3783.
- Lee K, Kivelson SA, Kim EA (2016) Cold-spots and glassy nematicity in underdoped cuprates. *arXiv:1603.03104*.
- Vignolle B, Vignolles D, Julien M-H, Proust C (2013) From quantum oscillations to charge order in high- $T_c$  copper oxides in high magnetic fields. *C R Phys* 14(1):39–52.
- da Silva Neto EH, et al. (2014) Ubiquitous interplay between charge ordering and high-temperature superconductivity in cuprates. *Science* 343(6169):393–396.
- Comin R, et al. (2014) Charge order driven by Fermi-arc instability in  $\text{Bi}_2\text{Sr}(2-x)\text{La}(x)\text{CuO}(6+\delta)$ . *Science* 343(6169):390–392.
- Blackburn E, et al. (2013) X-ray diffraction observations of a charge-density-wave order in superconducting ortho-II  $\text{YBa}_2\text{Cu}_3\text{O}_{6.54}$  single crystals in zero magnetic field. *Phys Rev Lett* 110(13):137004–137005.
- National Institute of Standards and Technology (2012) *NIST/SEMATECH e-Handbook of Statistical Methods* (National Institute of Standards and Technology, Gaithersburg, MD). Available at [www.itl.nist.gov/div898/handbook/leda/section3/normprpl.htm](http://www.itl.nist.gov/div898/handbook/leda/section3/normprpl.htm). Accessed July 1, 2016.
- Chambers JM, Cleveland WS, Tukey P, Kleiner B (1983) *Graphical Methods for Data Analysis* (Chapman and Hall, London).
- Lawler MJ, et al. (2010) Intra-unit-cell electronic nematicity of the high- $T_c$  copper-oxide pseudogap states. *Nature* 466(7304):347–351.
- Hamidian MH, et al. (2015) Magnetic-field induced interconversion of Cooper pairs and density wave states within cuprate composite order. *arXiv:1508.00620*.
- Kaneshita E, Martin I, Bishop AR (2007) Commensurate-incommensurate transition and associated collective modes in the stripe state of cuprates near 1/8 hole-doping. *Phys Rev B* 76(5):054507–1–054507-10.
- Bak P (1982) Commensurate phases, incommensurate phases and the devil's staircase. *Rep Prog Phys* 45(6):587–629.
- McMillan WL (1975) Landau theory of charge-density waves in transition-metal dichalcogenides. *Phys Rev B* 12(4):1187–1196.
- Achkar AJ, et al. (2014) Impact of quenched oxygen disorder on charge density wave order in  $\text{YBa}_2\text{Cu}_3\text{O}_{6+x}$ . *Phys Rev Lett* 113(10):107002–107005.